

# Polyacrylonitrile-based electrolytes: How processing and residual solvent affect ion transport and stability

Changhao Liu<sup>1</sup>, Robert L. Sacci<sup>1</sup>, Ritu Sahore<sup>1</sup>, Gabriel M. Veith<sup>1</sup>, Nancy J. Dudney<sup>1</sup>, X. Chelsea Chen<sup>1,\*</sup>

<sup>1</sup>Chemical Sciences Division, Oak Ridge National Laboratory, Oak Ridge, TN 37830, USA

This manuscript has been authored by UT-Battelle, LLC, under contract DE-AC05-00OR22725 with the US Department of Energy (DOE). The US government retains and the publisher, by accepting the article for publication, acknowledges that the US government retains a nonexclusive, paid-up, irrevocable, worldwide license to publish or reproduce the published form of this manuscript, or allow others to do so, for US government purposes. DOE will provide public access to these results of federally sponsored research in accordance with the DOE Public Access Plan

(<http://energy.gov/downloads/doe-public-access-plan>).

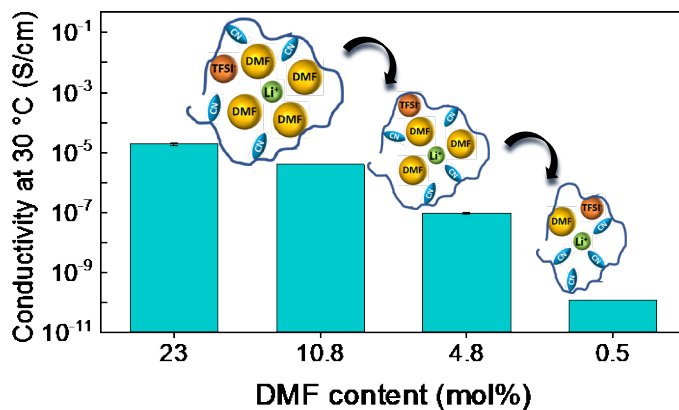
**\*Corresponding author**

**Email addresses: [chenx@ornl.gov](mailto:chenx@ornl.gov) (X. C. Chen)**

## Highlights

- Casting temperature affects the morphology of the PAN SPEs but does not strongly influence the ionic conductivity.  
Varying the drying temperature from room temperature to 120 °C causes 5 orders of magnitude decrease in the ionic conductivity .
- Li stability of PAN SPEs dramatically improves as the residual DMF content decreases.
- Oxidative stability of PAN SPEs is strongly affected by residual DMF content.
- Coordination structure and Li<sup>+</sup> conduction mechanism are determined by DMF content.

## Graphical Abstract



## Abstract

Polyacrylonitrile (PAN) is one of the alternative candidate polymer hosts to form solid polymer electrolytes (SPEs) besides the widely used poly(ethylene oxide). In this study, we systematically investigate the processing of PAN based SPEs containing lithium bis(trifluoromethanesulfonyl)imide (LiTFSI) salt, using dimethylformamide (DMF) as the solvent. The effects of PAN processing procedure including solution mixing, casting, and drying on the morphology, ion transport, solvation structure, Li and oxidative stability of PAN electrolytes are thoroughly examined. In particular, four drying conditions are investigated and the amount of residual DMF is accurately determined using infrared (IR) spectroscopy. Varying the drying conditions can lead to five orders of magnitude decrease in the ionic conductivity. As DMF content decreases, the SPE's stability against Li metal dramatically improves. The practical oxidative stability is also strongly affected by the residual DMF content, ranging from 2.5 V to 3.5 V, much lower than reported values. Finally, the role of the residual DMF solvent is elucidated. DMF content vitally influences ion solvation structure at different concentration regimes, which ultimately dictates the ion conduction

mechanism and oxidative stability of PAN based SPEs. This thorough study lays the groundwork for future development of PAN based electrolytes.

**Keywords:** polymer electrolyte, polyacrylonitrile, Li stability, electrochemical stability window, ion transport

## 1. Introduction

Solid polymer electrolytes (SPEs) are a promising class of solid-state electrolytes that may enable higher energy density batteries, particularly, the Li anode design[1]–[7]. Polyacrylonitrile (PAN) is one of the alternative candidate polymer hosts to form solid polymer electrolytes (SPEs) besides the widely used poly(ethylene oxide)[8]. The nitrile group makes PAN an excellent Lewis base to coordinate and solvate  $\text{Li}^+$  ions. To prepare PAN based SPEs, high dielectric constants solvent such as dimethyl formamide (DMF) are needed to dissolve PAN, followed by a drying step to remove the residual solvent. However, due to the high boiling point of these solvents and their strong coordination with  $\text{Li}^+$  ion, it is difficult to completely remove these solvent molecules. This leads to the question how the residual solvent influences ion solvation structure, ion transport mechanisms, ionic conductivity, and other electrochemical properties in in PAN based SPEs.

A discrepancy in the ionic conductivity of PAN based SPEs can be seen in the past literature reports. In Table 1 we summarize previously reported PAN based SPEs' conductivity. These reports all used solution casting method to prepare PAN based SPEs with DMF as the solvent. In both the low salt concentration and the high salt concentration regimes, an over 3 orders of magnitude of discrepancy in the ionic conductivity has been reported. The drying conditions and residual DMF content are seldom reported in these reports. because it is difficult to quantify the exact amount of DMF in PAN SPEs.

PAN based SPEs are known for their high oxidation stability up to 5.5 V[9], [10]. However, most published electrochemical stability window (ESW) measurements for PAN based electrolytes focus on gel

electrolytes[10]–[14]. The measured ESW values can vary dramatically depending on factors including the type of working electrodes used, temperature, and the measuring method [15]. Stability against Li metal is another important requirement for SPEs. Although PAN based electrolytes are typically considered unstable against Li, contradictory findings on Li stability have been reported. In a recent publication, PAN fiber array was electrospun onto Cu current collector to guide a uniform lithium deposition for a stable Li metal anode [16].

Given the aforementioned knowledge gaps, we systematically investigated the processing of PAN based electrolytes in this work. We focus on P(AN)<sub>6</sub>-LiTFSI SPE using DMF as the processing solvent. The condition of each processing step including solution mixing, casting, and drying is thoroughly examined. The effects of processing conditions on the morphology and ion transport properties of PAN based SPEs were evaluated. We identified that the casting temperature affects the morphology of the PAN SPEs but does not strongly influence the ionic conductivity. We report that the amount of residual solvent can be accurately determined by IR spectroscopy. Varying the drying temperature from room temperature to 120 °C causes 5 orders of magnitude decrease in the ionic conductivity. The stability of PAN SPEs against Li metal and ESW is evaluated as a function of the amount of residual DMF at 70 °C. Furthermore, the ion solvation structure, ion transport mechanism with regard to different processing conditions is elucidated by in-depth IR analyses. We report that the residual DMF content plays a critical role in the ion transport, stability against Li metal, and oxidative stability of PAN based SPEs. To our knowledge, such relationships have never been systematically examined. Through this work, we want to draw attention to the importance of quantifying residual solvent when processing polymer electrolytes such as PAN and polyvinylidene fluoride (PVDF), as it vitally influences transport and electrochemical properties.

*Table 1 Conductivity summary of PAN based SPEs from literatures<sup>(a)</sup>*

<b>PAN : salt molar ratio</b>	<b>Reported conductivity (S/cm)</b>	<b>Drying conditions</b>	<b>DMF residue</b>	<b>Ref.</b>
-------------------------------	-------------------------------------	--------------------------	--------------------	-------------

PAN : LiClO <sub>4</sub> = 6.67 : 1 PAN : LiClO <sub>4</sub> = 5 : 1	3.16 × 10 <sup>-8</sup> at 35 °C 3.16 × 10 <sup>-7</sup> at 35 °C	Not Reported (NR)	< 4.5 wt%	[17]
PAN : LiClO <sub>4</sub> = 4 : 1	1 × 10 <sup>-8</sup> at 30 °C	“Dried in a vacuum oven at a proper temperature for at least 24 ours”	< 10 wt%	[18]
PAN : LiClO <sub>4</sub> = 4 : 1	1 × 10 <sup>-7</sup> at 20 °C ~ 5 × 10 <sup>-7</sup> at 30 °C	Vacuum overnight. Temperature not specified	NR	[19]
PAN : LiClO <sub>4</sub> = 4 : 1	4.06 × 10 <sup>-7</sup> at 20 °C	Dried under vacuum over night at 50 °C	NR	[20]
PAN : LiClO <sub>4</sub> = 1.67 : 1	4 -- 5 × 10 <sup>-5</sup> at 30 °C	Dried under vacuum at 80 °C for at least 24 hours	NR	[21]
PAN : LiTFSI = 8 : 1	2.54 × 10 <sup>-4</sup> at 20 °C	The clear mixtures were cast on petri dishes and stored in the desiccator for at least 2 days until dry films were obtained.	NR	[22]
PAN : LiTFSI = 1 : 1	10 <sup>-5</sup> at 20 °C	Dried at 110 °C	NR	[23]
PAN : LiTFSI = 1 : 1	8 × 10 <sup>-5</sup> at 30 °C	Dried under vacuum. Temperature not specified	NR	[24]
LiCF <sub>3</sub> SO <sub>3</sub> concentration in PAN DMF solution from 10wt to 70wt%	10 <sup>-6</sup> to 10 <sup>-3</sup> at room temperature	Dried under vacuum for 48 hrs. Temperature not specified.	NR	[25]

PAN : LiTFSI = 6 : 1	$2.0 \times 10^{-5}$ (30 °C)	Air dry at 40 °C for 1 hr, under static vacuum at 23 °C for 14 hrs (Dry-A)	$23.4 \pm 0.7$ mol %	Current study
	$4.1 \times 10^{-6}$ (30 °C)	Air dry at 40 °C for 1 hr and 80 °C for 0.2 hrs, static vacuum dry at 23 °C for 14 hrs (Dry-B)	$11 \pm 2.5$ mol %	
	$9.6 \times 10^{-8}$ (30 °C)	Air dry at 40 °C for 1 hr and 80 °C for 2 hrs, dynamic vacuum dry at 80 °C for 14 hrs (Dry-C)	$5 \pm 0.5$ mol %	
	$1.2 \times 10^{-10}$ (30 °C)	Air dry at 40 °C for 1 hr and 80 °C for 2 hrs, dynamic vacuum dry at 120 °C for 65 hrs (Dry-D)	$0.5 \pm 0.2$ mol %	

(a) Note all of the cited reports used solution casting method to make PAN based electrolyte films and used DMF as the solvent.

## 2. Methods

### *Materials and preparation of PAN-based SPEs*

LiTFSI, LiClO<sub>4</sub>, PAN, and DMF were purchased from Sigma-Aldrich. LiTFSI and LiClO<sub>4</sub> were dried in a vacuum furnace at 120 °C inside an argon filled glovebox before use. For P(AN)<sub>6</sub>-LiTFSI, the solution was prepared by mixing LiTFSI, PAN in DMF at 120 °C using a stir bar on a hot plate, resulting in a 10 wt% solution (weight of PAN/(weight of PAN+ weight of DMF)) and a polymer to salt molar ratio of [CN] : [Li<sup>+</sup>] = 6 : 1. For P(AN)<sub>4</sub>-LiClO<sub>4</sub>, the dissolution temperature was 90 °C and the polymer to salt molar ratio was [CN] : [Li<sup>+</sup>] = 4 : 1. SPE films were cast on a copper foil using a doctor blade. Dried films had a thickness of around 70 μm. The samples were first air dried followed by further drying under vacuum (-

650 mmHg) at specific temperatures and time to control the amount of DMF residue. Details of sample drying will be discussed in the subsequent sections.

### *Infrared spectroscopy*

A Bruker INVENIO R spectrometer was used for IR measurement. IR samples were prepared in an argon filled glovebox, sealed between the ATR crystal and an airtight clamp with pressure applied. All measurements were conducted using a diamond crystal ATR accessory. Spectra were collected at a  $2\text{ cm}^{-1}$  resolution with 128 scans. Baseline correction, normalization, peak integration, and peak deconvolution were carried out in the software *OriginPro*. No ATR correction was performed for all the spectra. For peaking fitting, the Pseudo-Voigt function was used to model peak shape.

### *Electrochemical measurement*

**Electrochemical impedance spectroscopy (EIS)**, EIS was performed using a BioLogic potentiostat scanning from 100 mHz to 7 MHz. Two stainless steel rods were used as the blocking electrodes (note one side had copper as the substrate). The SPE film was sandwiched between the stainless steel rods and the cell was sealed with two layers of heat-shrink tubing. Temperature dependent EIS was measured in the temperature range from 20 °C to 100 °C with a 10 °C interval. The samples were equilibrated at each temperature for one hour before each measurement. Four cycles of temperature dependent EIS measurement were carried out (heat-cool-heat-cool). The first heating was for forming good contact and eliminating thermal history. Data from the last three cycles were used for conductivity calculation.

**Electrochemical stability window (ESW)**: ESWs of PAN based SPEs were determined at 70 °C by potentiostatic holds method using a Biologic potentiostat [26]. A cell was assembled using a polished Mo (Molybdenum) foil as working electrode and Li foil as both the reference and counter electrode. Three stainless steel spacers were used to guarantee a good contact between SPE and electrodes. For all samples, a two-hour resting time at 70 °C was given before measurement to enable good contact between SPE and electrode interface. EIS was immediately measured at OCV (open circuit voltage) to check the capacitance

of the SPE/Mo interface. For ESW measurement, two cells were used for the anodic and cathodic scans, respectively. Potentials were changed stepwise from OCV to 5 V (anodic scan) and from OCV to 0 V (cathodic scan) by a 0.1 V each step. At each step, voltage was held for a certain holding time depending on the current decay rate at each potential for each sample. The 6 min current value at each potential step was used for the current-potential plot.

**Measurement of SPE stability against Li metal:** the stability measurement was performed at 70 °C using a Li/Li symmetric cell. Time dependent EIS was monitored. The overall cell resistance extracted from Nyquist plot was used to create resistance-time plot.

**Measurement of Li<sup>+</sup> Transference number ( $t_+$ ):** Transference number measurements were taken using the Bruce and Vincent method with a Biologic VSP-300[27]. Li symmetric cells were equilibrated at 70 °C for 2 hours. After equilibration, the impedance was measured at open circuit voltage. Then chronoamperometric measurement was carried out at an applied potential ( $\Delta V$ ) of 10 mV for 2 hours. At the end of 2 hours' polarization time, the impedance was measured with the applied 10 mV potential. The chronoamperometry and the impedance measurements were repeated every 2 hours for a total of 10 hours. Transference number ( $t_+$ ) was then calculated using Equation 1. The initial current ( $I_0$ ) is calculated using Ohm's law  $\Delta V = I_0 \cdot R_0$ , where  $\Delta V = 10$  mV is the applied bias, and  $R_0$  is the total cell resistance obtained from the impedance spectrum prior to applying DC bias. Before each impedance measurement, the corresponding current ( $I_t$ ) is read from the chronoamperometry. The initial interfacial resistance,  $R_o$  was obtained by subtracting the electrolyte resistance from the total cell resistance, where the electrolyte resistance was calculated from the ionic conductivity and the geometry of the film. The interfacial resistance at time  $t$ ,  $R_t$  was obtained by subtracting the electrolyte resistance from the total cell resistance from the impedance spectra collected at time  $t$  with the applied bias (10 mV).

$$t_+ = \frac{I_t}{I_0} \left( \frac{\Delta V - I_0 R_0}{\Delta V - I_t R_t} \right) \quad (1)$$

### *Activation energy*

The activation energy ( $E_a$ ) was extracted from the temperature dependent conductivity data by fitting the Vogel–Tammann–Fulcher (VTF) equation,

$$\sigma = A \exp\left(-\frac{E_a}{k(T - T_0)}\right) \quad (2)$$

where  $\sigma$  (S/cm) is conductivity,  $A$  (S/cm) is the VTF prefactor,  $E_a$  (J) is activation energy,  $k$  is the Boltzmann constant, which is  $1.38 \times 10^{-23}$  J/K,  $T$  (K) is temperature, and  $T_0$  (K) is the Vogel temperature. Here, we adopted a similar VTF fitting protocol as Fit Routine 2 in the study of Diederichsen et al. [28]. Specifically,  $T_0$  was first found by maximizing the linearity of the plot of  $\log_{10} \sigma$  vs  $\frac{1000}{T - T_0}$  using the *LinearRegression* module from the *scikit-learn* package in Python. Integer between 0 and 299 was tested for  $T_0$  and the corresponding  $R^2$  (the coefficient of determination) for each fit was calculated. The  $T_0$  value with the highest  $R^2$  was adopted as the actual  $T_0$  to extract  $A$  and  $E_a$ . Fitted parameters for all the conductivity data in this report are listed in Table S2.  $A$  and  $E_a$  fitted from Arrhenius equation was also provided in Table S2 for comparison.

### *Scanning electron microscopy*

A Hitachi TM3030Plus tabletop scanning electron microscopy was used with a 15 kV acceleration voltage.

## **3. Results**

### **3.1 The effects of solution mixing and casting on the morphology and conductivity of PAN SPEs.**

Since the strong interactions between LiTFSI and DMF may cause PAN to crash out of the solution[29], higher temperatures are needed to make a homogeneous PAN-LiTFSI-DMF solution. Our experimental results indicate that for a molar ratio of  $[\text{CN}] : [\text{Li}^+] = 6 : 1$  (denoted as P(AN)<sub>6</sub>-LiTFSI), and a PAN concentration of 10 wt%, 120 °C was necessary to make a homogeneous solution of PAN and

LiTFSI. The PAN-LiTFSI-DMF solution demonstrates aging and gelation behavior (Fig. S1). As salt concentration increases, gelation time significantly shortens to overnight for P(AN)<sub>4</sub>-LiTFSI. It is worth mentioning that in a comparison study using LiClO<sub>4</sub> as the salt, we found that LiClO<sub>4</sub> is less likely to crash PAN out of the solution and aging is much slower (for example, in Fig S1(b), P(AN)<sub>4</sub>-LiClO<sub>4</sub>-DMF mixture doesn't gel overnight whereas P(AN)<sub>4</sub>-LiTFSI-DMF gels). In this work we chose P(AN)<sub>6</sub>-LiTFSI for further investigation due to its homogenous mixing in DMF and slow gelation behavior. We did not choose LiClO<sub>4</sub> as the salt due to safety concerns[30], [31].

After the PAN-LiTFSI-DMF formed a homogeneous solution, it was cooled down to room temperature and immediately cast onto a piece of copper foil placed on a heated aluminum plate, using a doctor blade. As shown in Fig. 1, the casting temperature (the set point temperature of the heated aluminum plate) dramatically affects the films' optical transparency and morphology. Hu et al. reported PAN-LiClO<sub>4</sub> films prepared by solution casting appears to be transparent [32]. In other literatures we searched, the film morphology was not reported.

Three casting temperatures were investigated, 120 °C, 80 °C and 40 °C. At a casting temperature of 120 °C, P(AN)<sub>6</sub>-LiTFSI showed a wavy texture with poor uniformity (Fig. 1a). Both opaque and transparent areas can be seen. Large oval shaped domains of the size of 1-2 mm were observed from the SEM image. Gaps and pinholes were present between these oval domains. The film cast at 80 °C also exhibited a wavy surface texture but much more uniform than the film cast at 120 °C (Fig. 1b). Similar sized domains were observed on this film, except that there were no gaps or pinholes between the domains. We hypothesize that the phase-separation like morphology associated with high casting temperatures is likely due to the precipitation of PAN caused by a more rapid removal of solvent at high temperatures. Casting at 40 °C, the film showed a flat surface but a translucent milky color (Fig. 1c). Casting at 40 °C followed by drying on the substrate at 80 °C for 2 hours, the film became transparent with a smooth surface (Fig. 1d). No oval shaped domains were observed on films cast at 40 °C. For all the casting conditions, the morphology at sub

100  $\mu\text{m}$  scale level appeared to be very similar. The surface of the films has a porous morphology. It is worth mentioning that  $\text{P}(\text{AN})_6\text{-LiTFSI}$  films are noticeably more brittle than neat PAN films.

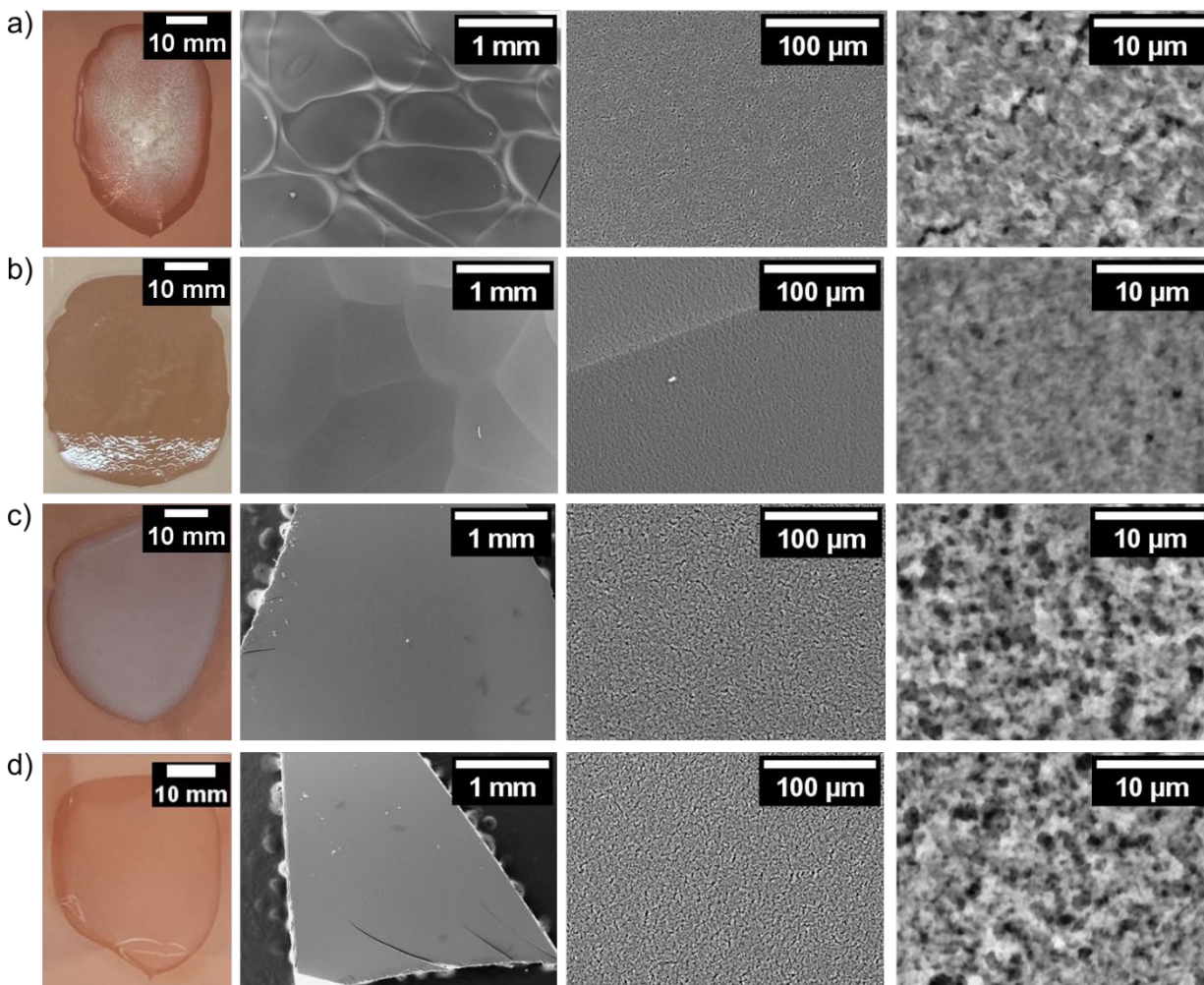


*Figure 1 Morphologies of  $\text{P}(\text{AN})_6\text{-LiTFSI}$  SPEs prepared by different casting conditions. a) cast at 120 °C. b) cast at 80 °C. c) cast at 40 °C. d) cast at 40 °C followed by further drying at 80 °C in air. All the samples were then vacuum dried at 80 °C for 14 hours.*

The ionic conductivity of  $\text{P}(\text{AN})_6\text{-LiTFSI}$  films cast at different temperatures is shown in Fig.2. The conductivity at 20 °C is  $2.7 \times 10^{-8}$  S/cm (cast at 40 °C),  $4.5 \times 10^{-8}$  S/cm (cast at 80 °C), and  $6.4 \times 10^{-8}$  S/cm (cast at 120 °C), respectively. Note the 40 °C sample in Fig.2 corresponds to the film in Fig.1d. The  $E_a$  of these samples was obtained by fitting the conductivity using VTF equation, following the protocol reported by Diederichsen et al. [28]. The  $E_a$  for cast at 120 °C is 0.27 eV, which is higher than that cast at 80 °C

(0.17 eV) and 40 °C (0.16 eV). All the  $E_a$  values are listed in Table S2. Overall, though varying casting conditions result in different film morphology, the resulting conductivity change is minimal, given the same drying conditions.

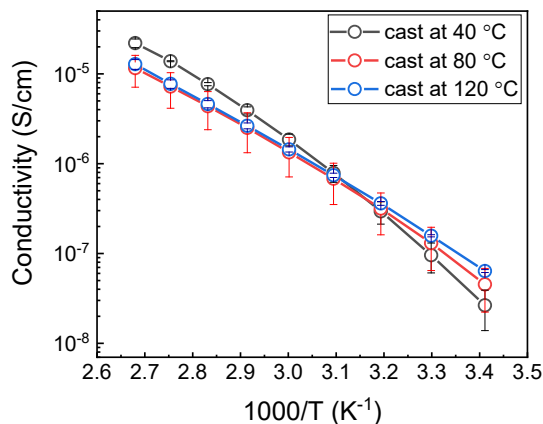


Figure 2 Conductivity as a function of  $1000/T$  for  $P(\text{AN})_6\text{-LiTFSI}$  SPEs prepared by different casting conditions. All the samples were dried at 80 °C under vacuum for 14 hours. Three films have the same DMF content (4.8 mol%).

### 3.2 The effects of drying conditions on residual DMF content and ion transport properties.

Four drying conditions, from Dry-A to Dry-D, were investigated on  $P(\text{AN})_6\text{-LiTFSI}$  SPEs. The details of different drying conditions are described in Table 1. The same casting temperature, 40 °C, was used for the drying experiments. DMF's boiling point is 153 °C at 760 mmHg, and its vapor pressure at 20 °C is 2.6 mmHg [33]. As a reference, water's vapor pressure at 20 °C is 17.5 mmHg [34]. The presence of  $\text{Li}^+$  is expected to further elevate DMF boiling point due to DMF/ $\text{Li}^+$  interaction [35]. Therefore, DMF is difficult to completely remove from a polymer electrolyte. Herein we use IR to accurately determine the DMF content in each film.

Fig. 3a shows IR spectra of  $P(\text{AN})_6\text{-LiTFSI}$  SPEs with drying conditions Dry-A to D. The signature peak of PAN is from the CN stretching region (2200  $\text{cm}^{-1}$  and 2300  $\text{cm}^{-1}$ ). The signature peak for DMF is located near 1660  $\text{cm}^{-1}$ , which is the  $\text{-C=O}$  stretching region. Note that LiTFSI does not have signature

peaks in these two regions. The molecular structure of PAN, DMF and LiTFSI is shown in the inset of Fig. 3a. Based on the Beer-Lambert law [36],

$$A_{CN} = \alpha_{CN} \cdot l \cdot c_{CN} \quad (3)$$

$$A_{CO} = \alpha_{CO} \cdot l \cdot c_{CO} \quad (4)$$

Where  $A_{CN}$  is integrated peak intensity for the CN signature peak;  $\alpha_{CN}$  is the absorption coefficient of CN species ( $\text{cm}^2/\text{mol}$ ),  $l$  is the penetration depth (cm), and  $c_{CN}$  is the molar concentration of CN species ( $\text{mol}/\text{cm}^3$ ). Similarly,  $A_{CO}$ ,  $\alpha_{CO}$ , and  $c_{CO}$  are the integrated peak intensity, the absorption coefficient and the molar concentration of CO species, respectively. The concentration ratio of CO to CN can be obtained by Equation 5. Since PAN and DMF coexist in the same film, the molar concentration ratio of CO to CN is equal to the molar ratio of DMF to CN groups. Equation 5 can be rewritten as Equation 6, where  $n_{DMF}$  and  $n_{CN}$  are the number of DMF molecules and CN groups in the SPE film, respectively, and  $k$  is a constant which is equal to  $\alpha_{CN}/\alpha_{CO}$ .

$$\frac{c_{CO}}{c_{CN}} = \frac{A_{CO}}{A_{CN}} \cdot \frac{\alpha_{CN}}{\alpha_{CO}} \quad (5)$$

$$\frac{n_{DMF}}{n_{CN}} = k \cdot \frac{A_{CO}}{A_{CN}} \quad (6)$$

The residual DMF content can thus be calculated from Equation 5, by measuring the ratio of the integrated peak intensity of CO and CN. The constant  $k = 0.012$ , determined by making standard solutions of PAN in DMF with known concentrations. The calculation of  $k$  is shown in Fig. S2.

In Fig.3a the CN peak intensity at  $2242 \text{ cm}^{-1}$  was normalized to 1 in all the spectra. As the drying condition gets more rigorous from Dry-A to Dry-D, it is evident that  $A_{CO}$  decreased, indicating a decrease in the residual DMF in the SPE films. The DMF residue was expressed in two terms, the molar fraction of DMF,  $\frac{n_{DMF}}{n_{DMF}+n_{LiTFSI}+n_{CN}}$ , shown in Table 1 and Fig. 3b; and molar ratio of DMF,  $n_{DMF}:n_{LiTFSI}:n_{CN}$ , shown in Table S1. Based on the pressure-temperature nomograph [37], the boiling point for DMF at a vacuum

level of -650 mmHg is estimated to be 89 °C. Drying overnight at 80 °C left 4.8 mol% residual DMF in the film (Dry-C). Drying below 80 °C or for shorter time period significantly increases the residual DMF content (Dry-A and Dry-B). Drying Increasing the drying temperature to 120 °C for as long as 65 hours resulted in 0.5 mol% DMF (Dry-D). In the literature reports cited in Table 1, the drying temperature is between 50 °C to 110 °C, or unspecified. Our drying conditions cover the range of most commonly used processing conditions to dry PAN SPEs. Since polar solvents may cause PAN to degrade at a relatively low temperature [38], we did not attempt to process PAN films higher than 120 °C, to avoid degradation.

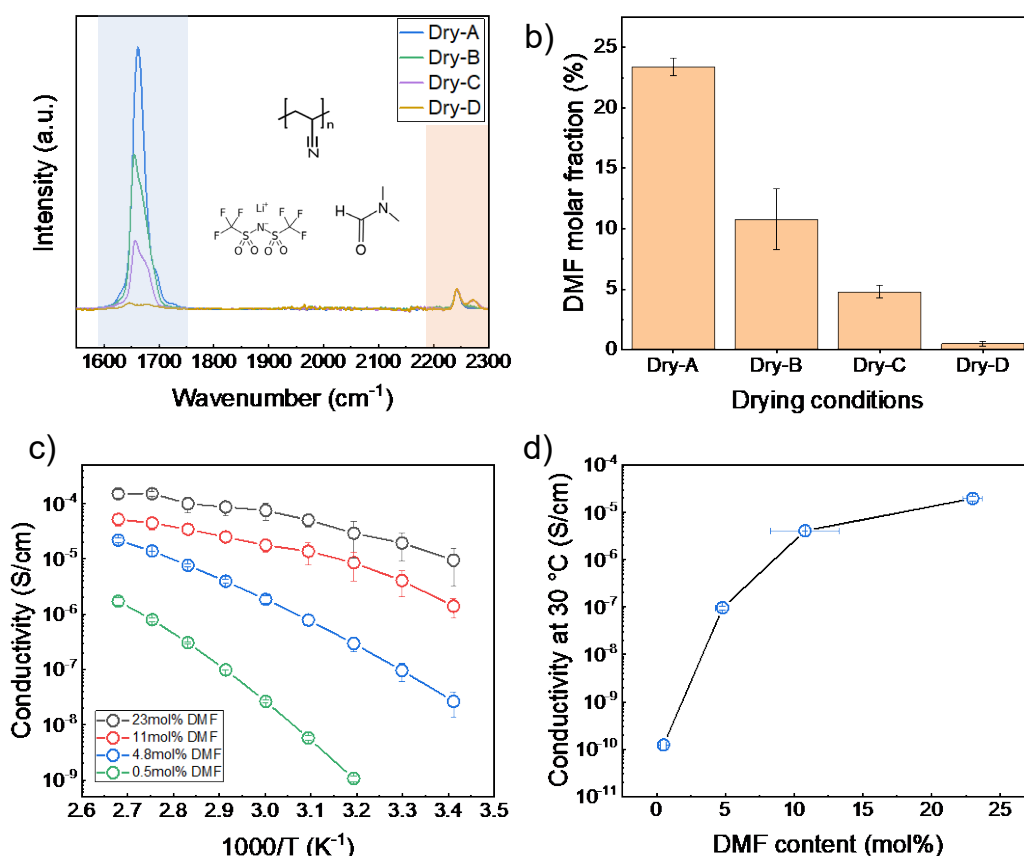


Figure 3 (a) C=O and CN regions of IR spectra for P(AN)<sub>6</sub>-LiTFSI SPEs as a function of drying conditions. Spectra were normalized to the uncoordinated CN peak. (b) the amount of DMF residue as a function of drying conditions. (c) Conductivity as a function of 1000/T for P(AN)<sub>6</sub>-LiTFSI SPEs with drying conditions A-D. (d). Conductivity at 30 °C as a function of residual DMF molar percentage. Note the conductivity value at 30 °C for the 0.5 mol% DMF sample is extrapolated from VTF fitting.

The ionic conductivity of P(AN)<sub>6</sub>-LiTFSI SPEs using Dry-A to D conditions was measured and plotted as a function of inverse temperature in Fig. 3c. The Nyquist plot for each sample at different

temperatures are shown in Fig. S5. As can be seen, more than 5 orders of magnitude difference in conductivity near room temperature is obtained, depending on the residual DMF content. The  $E_a$  (VTF fit) for Dry-A and Dry-B are 0.03 eV and 0.02 eV. There is a noticeable increase in the  $E_a$  for Dry-C (0.16 eV), and Dry-D (0.19 eV) as DMF content decreases. These results clearly illustrate that the drying conditions and residual DMF content critically influence the conductivity in the final SPEs. Notably, there is a 3 orders of magnitude difference in conductivity at 30 °C between drying condition Dry-C ( $9.6 \times 10^{-8}$  S/cm, vacuum 80 °C for 14 hrs) and Dry-D ( $1.2 \times 10^{-10}$  S/cm, vacuum 120 °C for 65 hrs), as shown in Fig. 4b. According to literature, both these conditions can be referred to as “thoroughly dried”. However, the last few mole percent of residual DMF plays a critical role in the transport mechanism of PAN SPEs.

The  $\text{Li}^+$  transference number ( $t_+$ ) of  $\text{P}(\text{AN})_6\text{-LiTFSI}$  using drying conditions Dry-A to Dry-C was measured using the Bruce-Vincent method by constructing Li symmetric cells[27]. Dry-D film was too resistive to be measured using this method. The results are shown in Fig. S3. Due to the continuous reaction between  $\text{P}(\text{AN})_6\text{-LiTFSI}$  and Li, a steady state current could not be reached during the chronoamperometry measurement. As a result, a steady-state  $t_+$  could not be obtained. Furthermore, due to the large interfacial resistance between  $\text{P}(\text{AN})_6\text{-LiTFSI}$  and Li,  $t_+$  values obtained using this method is low. Dry-A,  $t_+$  ranges from 0.002 to 0.006; Dry-B,  $t_+$  ranges from 0.02 to 0.07; Dry-D,  $t_+$  ranges from 0.06 to 0.09. The values were obtained between 2 to 10 hours of equilibration time with the applied bias.

### 3.3 The effects of residual DMF content on Li and oxidative stability.

The stability of  $\text{P}(\text{AN})_6\text{-LiTFSI}$  SPEs against Li metal was assessed by measuring the Li symmetric cell resistance as a function of time at 70 °C. Figs. 4a-d show the Nyquist plots at different times for different drying conditions. The total cell resistance is determined by the value of the Nyquist plot’s low frequency touchdown on the  $\text{Re}(Z)$  axis. Figs. 4e-f show normalized cell resistance  $R/R_0$  as a function of time, where  $R$  is the cell resistance at time  $t$  and  $R_0$  is the initial cell resistance after equilibrating at 70 °C for 2 hours.

We see for Dry-A and Dry-B the cell resistance increased rapidly over just 25 hours of time whereas for Dry-C and Dry-D, the resistance initially decreased then increased much more slowly. The initial decrease in cell resistance was due to the formation of better contact with Li electrodes. After 25 hours, the resistance of Dry-A and Dry-B increased by 51 times and 50 times, respectively, whereas after 250 hours the resistance of Dry-C and Dry-D increased by 7.5 times and 3.4 times, respectively. This result shows that residual DMF plays an important role in the Li stability of PAN based SPEs. By reducing the DMF content of PAN SPE films, improved Li stability can be achieved.

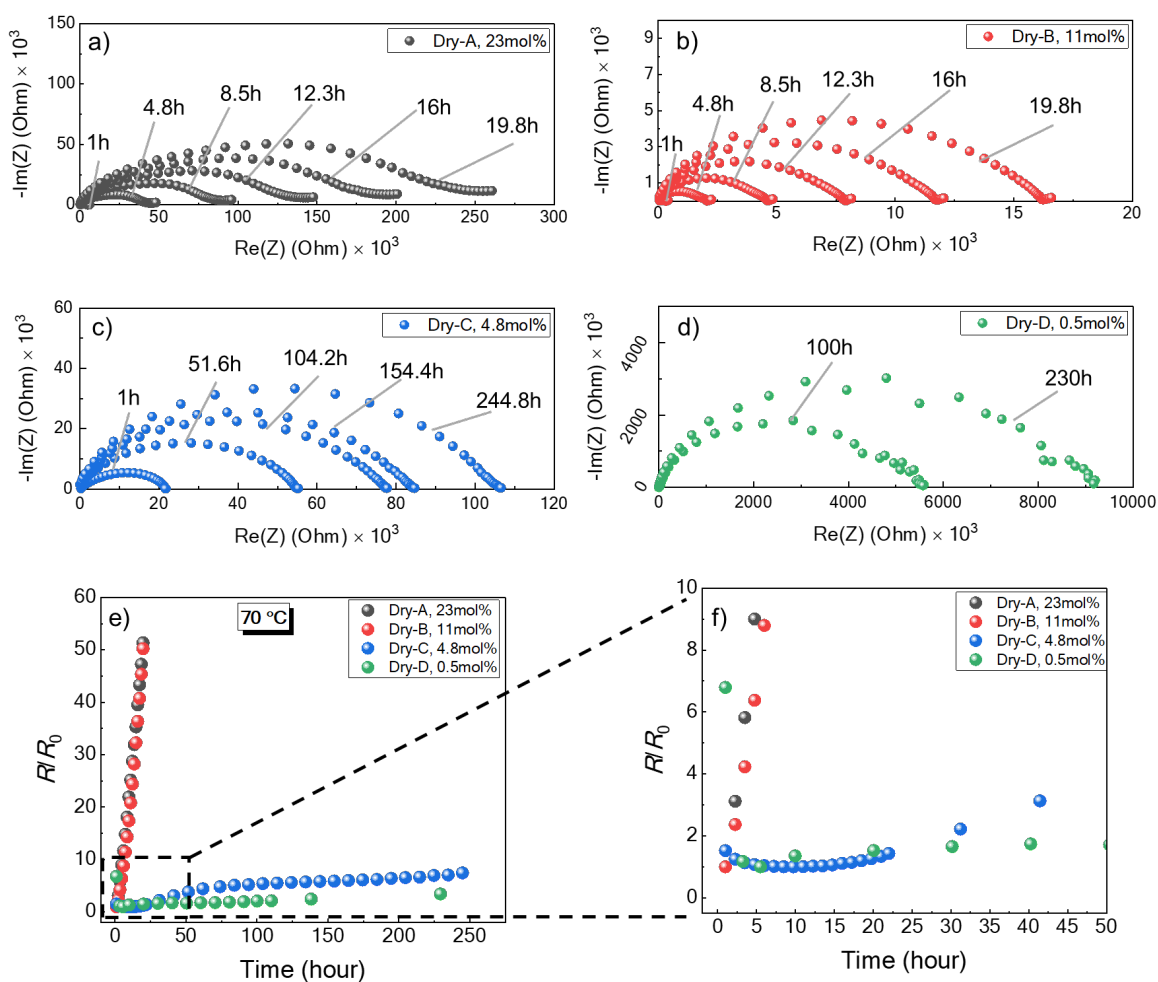


Figure 4 (a – d), Nyquist plot showing Li symmetric cell resistance as a function of time for P(AN)<sub>6</sub>-LiTFSI SPEs with different drying conditions corresponding to Dry-A to Dry-D. The impedance measurements were done at 70 °C. (e), Normalized cell resistance as a function of time at 70 °C with different drying conditions; (f) enlarged area of (e) before 50 hours.

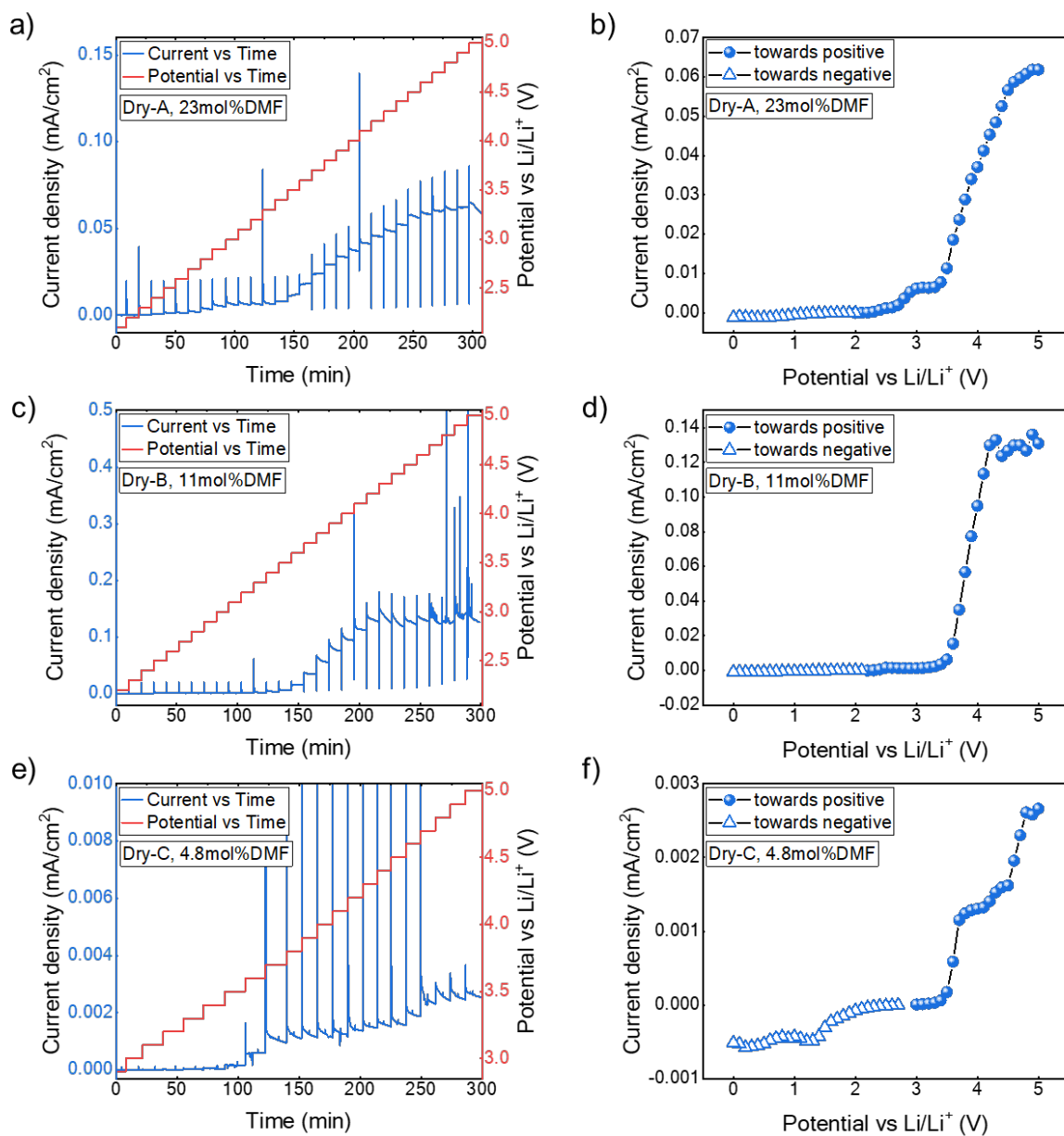


Figure 5 The potentiostat hold method to determine the electrochemical stability window of  $P(AN)_6\text{-LiTFSI}$ . (a), (c), (e) Current density vs time (left vertical axis) and potential vs time (right vertical axis) for different drying conditions Dry-A, Dry-B, and Dry-C. The hold time at each voltage step was 6 min. (b) (d) (f) Current density at 6 min vs potential time for different drying conditions Dry-A, Dry-B, and Dry-C.

The oxidative stability of  $P(AN)_6\text{-LiTFSI}$  was measured in a Li/Mo cell at 70 °C using a potentiostat hold method, which is considered to provide more accurate and practical ESW results [15], [26]. Different than the conventional cyclic voltammetry measurements, the potentiostat hold technique allows the sample to stay at each potential step for a period of time to equilibrate before jumping to the next potential. Fig. 5 shows potentiostat hold results for the three different samples, Dry-A, Dry-B, and Dry-C.

We didn't examine the Dry-D sample since its conductivity is extremely low. The samples were allowed to hold for 6 min under each voltage step. It's worth mentioning that changing the hold time from 6 min to 1 hour did not change the results. For Dry-A condition, the onset of first oxidative event occurred at as low as 2.8 V. A second oxidative event occurred at 3.5 V. The oxidative event at 2.8 V corresponds to the reaction of free DMF molecules[35]. The oxidative event at 3.5 V corresponds to the oxidation of bound DMF. (add ref) For Dry-B condition, the same oxidation event at 3.5 V was observed. For Dry-C condition, the first oxidative event occurred at 3.5 V, similar to Dry-B; then another oxidative event at 4.5 V was observed, which corresponds to the oxidation of PAN. (Add ref) On the reductive side, the results are inconclusive using the Li||Mo cell design because of the continuous reaction on the Li electrode (Fig. 4).

### 3.4 The effects of residual DMF content on Li<sup>+</sup> solvation structure.

The Li<sup>+</sup> solvation structure in P(AN)<sub>6</sub>-LiTFSI can be elucidated by examining three corresponding spectral regions in IR: 1) C=O stretching between 1600 and 1750 cm<sup>-1</sup>. This region reveals Li<sup>+</sup> solvation from DMF's oxygen. 2) CH<sub>3</sub> rocking between 1020 and 1120 cm<sup>-1</sup>. This region reveals Li<sup>+</sup> solvation from DMF's nitrogen [39]. 3) CN stretching between 2220 and 2290 cm<sup>-1</sup>. This region reveals Li<sup>+</sup> solvation from PAN.

In order to elucidate the solvation structure as a function of residual DMF content, we first investigated the interaction between PAN and DMF without any salt, in the aforementioned three signature IR spectral regions, shown in Figs. 6a-c. In the carbonyl region (Fig. 6a), the C=O peak is located at 1660 cm<sup>-1</sup> for both neat DMF and 10 wt% PAN-DMF solution. In the PAN film dried with Dry-C condition (without salt), the C=O peak shifts to a higher wavenumber of 1667 cm<sup>-1</sup>. Such a blue shift suggests the C=O bond is shortened when DMF concentration decreases. In DMF self-association, weak H-bonding exists between C-H and C=O [40], whereas in PAN-DMF mixture, an antiparallel alignment of C=O and CN through dipole-dipole interaction exists [38].

In the CH<sub>3</sub> rocking region (Fig. 6b), both neat DMF and 10 wt% PAN-DMF solution have a peak at 1089 cm<sup>-1</sup>. This peak was assigned to the CH<sub>3</sub> rocking mode from DMF [39]. This peak slightly shifted to 1093 cm<sup>-1</sup> in PAN film dried by Dry-C. In the CN stretching region (Fig. 6c), all samples (without salt) show the same peak at 2242 cm<sup>-1</sup>, indicating no vibrational frequency shift for the CN group when DMF content decreases. These results indicate that DMF's structure only slightly changed in a PAN matrix, conversely PAN's structure was not significantly affected by the presence of residual DMF. This result is consistent with the result by Wu et al., wherein they show the binding energy of DMF-DMF pair is similar as DMF-PAN pair [38].

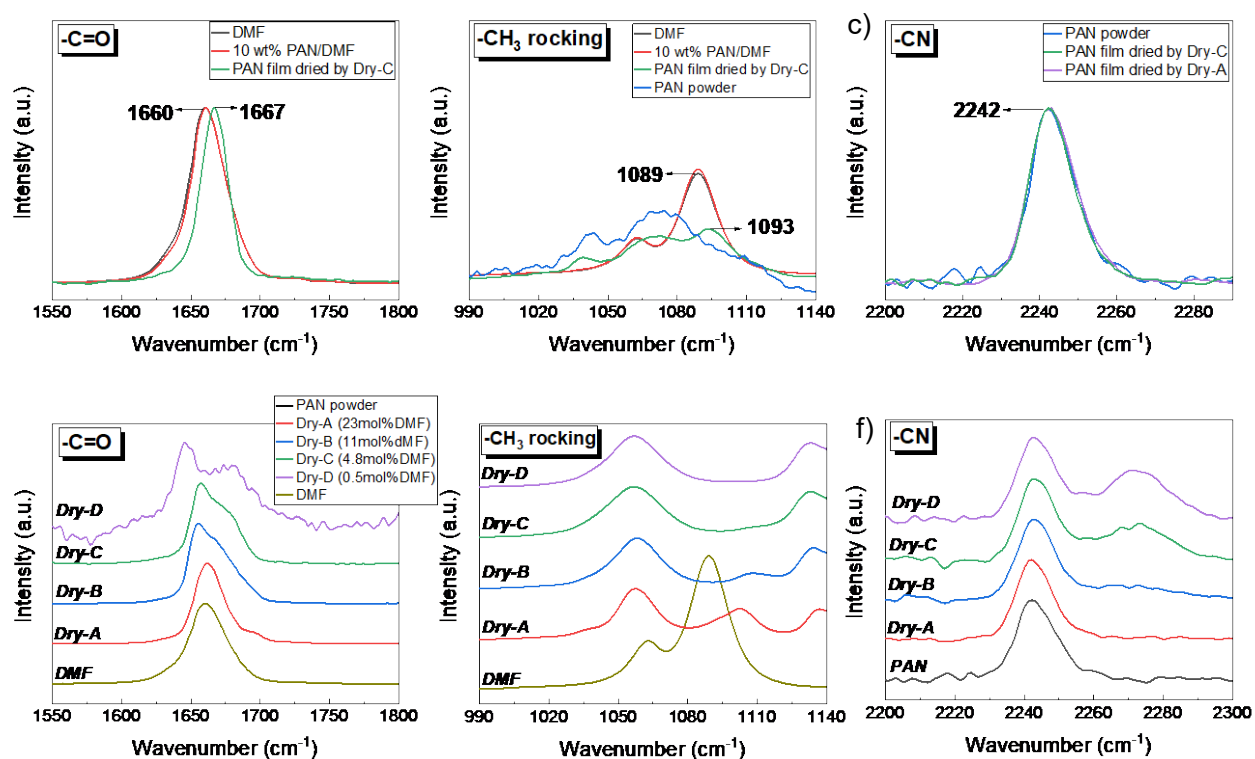


Figure 6 Using IR to elucidate the Li<sup>+</sup> solvation structure in P(AN)<sub>6</sub>-LiTFSI. (a-c), IR spectra of binary mixtures of PAN and DMF without any salt. a) carbonyl region of DMF, PAN-DMF 10 wt% PAN mixture, and PAN film dried by Dry-C. b) the CH<sub>3</sub> rocking region of DMF, PAN-DMF 10 wt% PAN mixture, PAN film dried by Dry-C, and PAN powder. c) PAN film dried by Dry-A, PAN film dried by Dry-C, and PAN powder. (d-f), IR spectra of P(AN)<sub>6</sub>-LiTFSI-DMF three-component system. a) carbonyl region, b) CH<sub>3</sub> rocking region, and c) CN region for PAN powder, DMF, Dry-A, Dry-B, Dry-C, and Dry-D of P(AN)<sub>6</sub>-LiTFSI SPEs.

Now we examine the P(AN)<sub>6</sub>-LiTFSI-DMF three-component system (Figs. 6d-f). A summary of IR peaks evolution as a function of residual DMF content is included in Table S3. With Dry-A condition and 23 mol% residual DMF, the C=O stretching band remained the same to that of neat DMF and the CN stretching band remained the same to that of neat PAN. On the other hand, the CH<sub>3</sub> rocking band shifted from neat DMF's 1089 cm<sup>-1</sup> to 1103 cm<sup>-1</sup>. The shift is due to the coordination between Li<sup>+</sup> and N(CH<sub>3</sub>)<sub>2</sub> in DMF [39]. Therefore, with relatively high DMF content, most of the Li<sup>+</sup> is coordinated with the amide nitrogen in DMF. PAN does not participate in ion transport.

With Dry-B condition and 11 mol% DMF, the C=O stretching band became asymmetric. Peak deconvolution (Fig.S4) reveals two components, located at 1655 cm<sup>-1</sup> and 1668 cm<sup>-1</sup>, respectively. The split of the C=O stretching band indicates two different local surroundings for DMF's carbonyl group. The 1655 cm<sup>-1</sup>, which is a substantial red shift from neat DMF's 1661 cm<sup>-1</sup>, is originated from the coordination between -C=O and Li<sup>+</sup>. The 1668 cm<sup>-1</sup> is from non-coordinated DMF. The blueshift is similar to PAN-DMF without salt, discussed earlier. The CH<sub>3</sub> rocking mode shifts towards a higher vibrational frequency of 1107 cm<sup>-1</sup>. In the CN stretching region, a very weak peak at 2272 cm<sup>-1</sup> can be observed. This peak is the signature peak of CN coordinating with Li<sup>+</sup> [41]. The low intensity suggests only a small number of CN groups coordinated with Li<sup>+</sup> at this DMF content. These results reveal that with medium DMF content, all three mechanisms for ion transport coexist, i.e., Li<sup>+</sup> coordination with DMF through N(CH<sub>3</sub>)<sub>2</sub>, Li<sup>+</sup> coordination with DMF through C=O, and Li<sup>+</sup> coordination with CN of PAN.

With Dry-C condition and 4.8 mol% DMF, C=O stretching is still a convolution of two peaks (Fig S4), representing Li<sup>+</sup> coordinated DMF and non-coordinated DMF. The coordinated DMF peak is located at 1655 cm<sup>-1</sup>. The non-coordinated DMF shifts to a higher frequency of 1673 cm<sup>-1</sup>. A very weak CH<sub>3</sub> rocking band of DMF was observed at 1108 cm<sup>-1</sup>. In the CN stretching region, the 2272 cm<sup>-1</sup> peak in the CN region becomes much stronger. In this relatively low DMF content regime, all three mechanisms for ion transport coexist. Compared to Dry-B condition, more PAN chains contribute to the coordination with Li<sup>+</sup> and hence ion transport.

With Dry-D condition and 0.5 mol% DMF, the C=O stretching region is a convolution of two peaks. The lower frequency peak shifts to 1646  $\text{cm}^{-1}$  whereas the higher frequency component shifts to 1677  $\text{cm}^{-1}$ . The  $\text{CH}_3$  rocking peak could not be observed due to an extremely low concentration of DMF. In the CN stretching region, the peak intensity of 2272  $\text{cm}^{-1}$  further increased, indicating with more DMF removed, more CN groups coordinated with  $\text{Li}^+$ .

#### 4. Discussion

To this end, a holistic picture of the  $\text{Li}^+$  solvation structure, ion transport mechanism, Li and oxidative stability of  $\text{P(AN)}_6\text{-LiTFSI}$  as a function of residual DMF content has emerged. Three regimes can be identified, shown in Fig. 7. In high DMF content regime ( $>23$  mol%),  $\text{Li}^+$  is solvated by DMF mainly through the  $\text{N-(CH}_3)_2$  group. PAN is only serving as a host for DMF and does not participate in ion conduction. This is consistent with the observed high room temperature conductivity and a low  $E_a$ . In this regime,  $\text{P(AN)}_6\text{-LiTFSI}$  exhibits very low oxidative stability (2.8 V). This is consistent with the low oxidative stability of free uncoordinated DMF[35]. Due to the presence of free DMF, very poor Li stability is also observed.

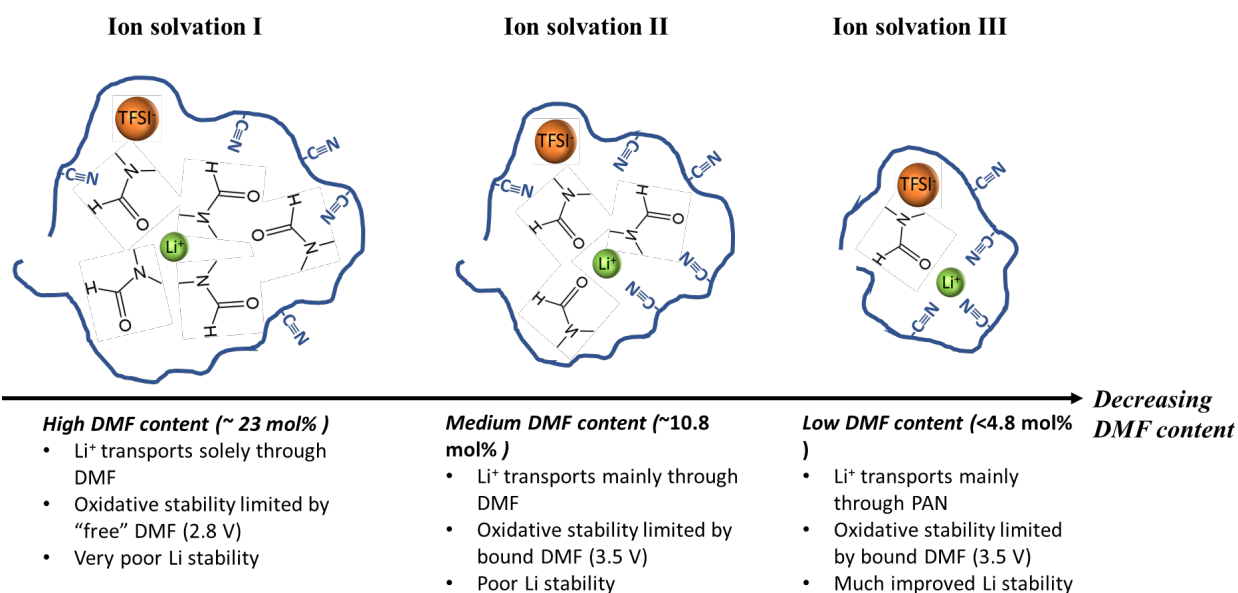


*Figure 7 The effect of DMF content on solvation structure, ion transport mechanism, Li and oxidative stability is elucidated. schematic illustration for the first solvation shell of Li<sup>+</sup> in different DMF content regimes. The solvation number was arbitrarily drawn only for illustration. Anions were not included.*

In the medium DMF content regime ((5 to 11 mol%), Li<sup>+</sup> transports through the coordination with DMF's N-(CH<sub>3</sub>)<sub>2</sub> as well as -C=O. A small amount of CN in PAN also contributes to the solvation of Li<sup>+</sup>. The oxidative stability of the SPE is 3.5 V, consistent with that of LiTFSI. (add ref). Poor Li stability is again observed. In the low DMF content regime (< 4.8 mol%), the solvation shell of Li<sup>+</sup> becomes PAN rich. PAN dominates Li<sup>+</sup> transport. Since the predominant ion transport relies on the chain segmental mobility of PAN, low conductivity and a high activation energy are observed. In this regime the oxidative stability is also limited by LiTFSI.

Overall, it is evident that ion transport in PAN electrolyte is always aided by DMF, even in the lowest DMF content (0.5 mol%). The Li stability increases with decreasing DMF content. Although PAN as a polymer host indeed has high oxidative stability, the oxidative stability of PAN electrolytes are subject to the choice of Li salt as well as DMF content. These findings lay the groundwork for developing PAN electrolyte based solid-state batteries.

## 5. Conclusions

In this work we systematically investigated the processing of P(AN)<sub>6</sub>-LiTFSI electrolyte using DMF as the processing solvent. We found the casting temperatures (40 °C, 80 °C, and 120 °C) result in different SPE morphology, but the ionic conductivity of the resulting films was not strongly affected, given the same drying conditions. In contrast, varying the vacuum drying temperature from room temperature to 120 °C causes a dramatic change in the conductivity, Li stability, and oxidative stability. FTIR can be used to quantify residual DMF content in PAN based SPEs. The molar concentration varies from 23 mol% (drying at room temperature) to 0.5 mol% (drying at 120 °C).

In the high DMF content regime, Li<sup>+</sup> is exclusively coordinated by DMF, mainly from the amide nitrogen. PAN does not contribute to ion conduction. In the medium DMF content regime, Li<sup>+</sup> is coordinated by both DMF and PAN. In the low DMF content regime, the majority of Li<sup>+</sup> coordination is

with PAN. Ionic conductivity decreases by more than 5 orders of magnitude from 23 mol% to 0.5 mol% DMF. As DMF content decreases, the stability of SPE against Li metal is improved. The oxidative stability increases from 2.8 V to 3.5 V, with decreasing DMF content. Across all concentration regimes, DMF plays an important role in ion solvation, conduction, and electrochemical stability window. Thus, it is very critical to quantify the residual DMF (or other high boiling point solvents) for PAN based SPEs for further development.

## Acknowledgements

This work was supported by the U. S. Department of Energy, Office of Science, Basic Energy Sciences, Materials Science and Engineering Division. We acknowledge discussion with Dr. Frank M. Delnick on the guidance on the potentiostat hold measurements.

## References

- [1] N. J. Dudney, W. C. West, and J. Nanda, *Handbook of solid state batteries*, vol. 6. World Scientific, 2015.
- [2] J. C. Bachman *et al.*, “Inorganic Solid-State Electrolytes for Lithium Batteries: Mechanisms and Properties Governing Ion Conduction,” *Chem. Rev.*, vol. 116, no. 1, pp. 140–162, Jan. 2016, doi: 10.1021/acs.chemrev.5b00563.
- [3] K. B. Hatzell *et al.*, “Challenges in Lithium Metal Anodes for Solid-State Batteries,” *ACS Energy Lett.*, vol. 5, no. 3, pp. 922–934, Mar. 2020, doi: 10.1021/acseenergylett.9b02668.
- [4] “Lithium Metal Anodes: Toward an Improved Understanding of Coupled Morphological, Electrochemical, and Mechanical Behavior | ACS Energy Letters.” <https://pubs.acs.org/doi/10.1021/acseenergylett.6b00650> (accessed Jun. 07, 2021).
- [5] L. Yue *et al.*, “All solid-state polymer electrolytes for high-performance lithium ion batteries,” *Energy Storage Materials*, vol. 5, pp. 139–164, Oct. 2016, doi: 10.1016/j.ensm.2016.07.003.
- [6] A. Mauger, M. Armand, C. M. Julien, and K. Zaghib, “Challenges and issues facing lithium metal for solid-state rechargeable batteries,” *Journal of Power Sources*, vol. 353, pp. 333–342, Jun. 2017, doi: 10.1016/j.jpowsour.2017.04.018.
- [7] “Polymer Electrolytes | Annual Review of Materials Research.” <https://www.annualreviews.org/doi/10.1146/annurev-matsci-071312-121705> (accessed Apr. 13, 2021).
- [8] J. Mindemark, M. J. Lacey, T. Bowden, and D. Brandell, “Beyond PEO—Alternative host materials for Li + -conducting solid polymer electrolytes,” *Progress in Polymer Science*, vol. 81, pp. 114–143, Jun. 2018, doi: 10.1016/j.progpolymsci.2017.12.004.

- [9] P. Hu, J. Chai, Y. Duan, Z. Liu, G. Cui, and L. Chen, "Progress in nitrile-based polymer electrolytes for high performance lithium batteries," *J. Mater. Chem. A*, vol. 4, no. 26, pp. 10070–10083, 2016, doi: 10.1039/C6TA02907H.
- [10] S. Panero, D. Satolli, A. D'Epifano, and B. Scrosati, "High Voltage Lithium Polymer Cells Using a PAN-Based Composite Electrolyte," *J. Electrochem. Soc.*, vol. 149, no. 4, p. A414, Feb. 2002, doi: 10.1149/1.1454139.
- [11] G. B. Appetecchi, F. Croce, P. Romagnoli, B. Scrosati, U. Heider, and R. Oesten, "High-performance gel-type lithium electrolyte membranes," *Electrochemistry Communications*, vol. 1, no. 2, pp. 83–86, Feb. 1999, doi: 10.1016/S1388-2481(99)00011-9.
- [12] H. Akashi, M. Shibuya, K. Orui, G. Shibamoto, and K. Sekai, "Practical performances of Li-ion polymer batteries with LiNi<sub>0.8</sub>Co<sub>0.2</sub>O<sub>2</sub>, MCMB, and PAN-based gel electrolyte," *Journal of Power Sources*, vol. 112, no. 2, pp. 577–582, Nov. 2002, doi: 10.1016/S0378-7753(02)00465-2.
- [13] P. Raghavan, J. Manuel, X. Zhao, D.-S. Kim, J.-H. Ahn, and C. Nah, "Preparation and electrochemical characterization of gel polymer electrolyte based on electrospun polyacrylonitrile nonwoven membranes for lithium batteries," *Journal of Power Sources*, vol. 196, no. 16, pp. 6742–6749, Aug. 2011, doi: 10.1016/j.jpowsour.2010.10.089.
- [14] H.-R. Jung, D.-H. Ju, W.-J. Lee, X. Zhang, and R. Kotek, "Electrospun hydrophilic fumed silica/polyacrylonitrile nanofiber-based composite electrolyte membranes," *Electrochimica Acta*, vol. 54, no. 13, pp. 3630–3637, May 2009, doi: 10.1016/j.electacta.2009.01.039.
- [15] A. Méry, S. Rousselot, D. Lepage, and M. Dollé, "A Critical Review for an Accurate Electrochemical Stability Window Measurement of Solid Polymer and Composite Electrolytes," *Materials*, vol. 14, no. 14, Art. no. 14, Jan. 2021, doi: 10.3390/ma14143840.
- [16] "Uniform Lithium Deposition Induced by Polyacrylonitrile Submicron Fiber Array for Stable Lithium Metal Anode | ACS Applied Materials & Interfaces." <https://pubs.acs.org/doi/abs/10.1021/acsami.7b00181> (accessed Oct. 25, 2021).
- [17] C. R. Yang, J. T. Perng, Y. Y. Wang, and C. C. Wan, "Conductive behaviour of lithium ions in polyacrylonitrile," *Journal of Power Sources*, vol. 62, no. 1, pp. 89–93, Sep. 1996, doi: 10.1016/S0378-7753(96)02414-7.
- [18] Y. W. Chen-Yang, H. C. Chen, F. J. Lin, and C. C. Chen, "Polyacrylonitrile electrolytes 1. A novel high-conductivity composite polymer electrolyte based on PAN, LiClO<sub>4</sub> and a-Al<sub>2</sub>O<sub>3</sub>," *Solid State Ionics*, p. 9, 2002.
- [19] W. Liu *et al.*, "Ionic Conductivity Enhancement of Polymer Electrolytes with Ceramic Nanowire Fillers," *Nano Lett.*, vol. 15, no. 4, pp. 2740–2745, Apr. 2015, doi: 10.1021/acs.nanolett.5b00600.
- [20] T. Yang, J. Zheng, Q. Cheng, Y.-Y. Hu, and C. K. Chan, "Composite Polymer Electrolytes with Li<sub>7</sub>La<sub>3</sub>Zr<sub>2</sub>O<sub>12</sub> Garnet-Type Nanowires as Ceramic Fillers: Mechanism of Conductivity Enhancement and Role of Doping and Morphology," *ACS Appl. Mater. Interfaces*, vol. 9, no. 26, pp. 21773–21780, Jul. 2017, doi: 10.1021/acsami.7b03806.
- [21] Y. T. Chen, Y. C. Chuang, J. H. Su, H. C. Yu, and Y. W. Chen-Yang, "High discharge capacity solid composite polymer electrolyte lithium battery," *Journal of Power Sources*, vol. 196, no. 5, pp. 2802–2809, Mar. 2011, doi: 10.1016/j.jpowsour.2010.11.058.
- [22] L. N. Sim, F. C. Sentanin, A. Pawlicka, R. Yahya, and A. K. Arof, "Development of polyacrylonitrile-based polymer electrolytes incorporated with lithium bis(trifluoromethane)sulfonimide for application in electrochromic device," *Electrochimica Acta*, vol. 229, pp. 22–30, Mar. 2017, doi: 10.1016/j.electacta.2017.01.098.
- [23] B. Wu *et al.*, "Performance of 'Polymer-in-Salt' Electrolyte PAN-LiTFSI Enhanced by Graphene Oxide Filler," *J. Electrochem. Soc.*, vol. 163, no. 10, pp. A2248–A2252, 2016, doi: 10.1149/2.0531610jes.
- [24] H. Gao, N. S. Grundish, Y. Zhao, A. Zhou, and J. B. Goodenough, "Formation of Stable Interphase of Polymer-in-Salt Electrolyte in All-Solid-State Lithium Batteries," *Energy Material Advances*, vol. 2021, pp. 1–10, Jan. 2021, doi: 10.34133/2021/1932952.

- [25] H.-K. Yoon, W.-S. Chung, and N.-J. Jo, "Study on ionic transport mechanism and interactions between salt and polymer chain in PAN based solid polymer electrolytes containing LiCF<sub>3</sub>SO<sub>3</sub>," *Electrochimica Acta*, vol. 50, no. 2–3, pp. 289–293, Nov. 2004, doi: 10.1016/j.electacta.2004.01.095.
- [26] C. V. Amanchukwu, Z. Yu, X. Kong, J. Qin, Y. Cui, and Z. Bao, "A New Class of Ionically Conducting Fluorinated Ether Electrolytes with High Electrochemical Stability," *J. Am. Chem. Soc.*, vol. 142, no. 16, pp. 7393–7403, Apr. 2020, doi: 10.1021/jacs.9b11056.
- [27] J. Evans, C. A. Vincent, and P. G. Bruce, "Electrochemical measurement of transference numbers in polymer electrolytes," *Polymer*, vol. 28, no. 13, pp. 2324–2328, Dec. 1987, doi: 10.1016/0032-3861(87)90394-6.
- [28] K. M. Diederichsen, H. G. Buss, and B. D. McCloskey, "The Compensation Effect in the Vogel–Tammann–Fulcher (VTF) Equation for Polymer-Based Electrolytes," *Macromolecules*, vol. 50, no. 10, pp. 3831–3840, May 2017, doi: 10.1021/acs.macromol.7b00423.
- [29] Z. Wang, W. Gao, X. Huang, Y. Mo, and L. Chen, "Influence of Salt Content on Polymer Dissolution and Ionic Association in Polymer Electrolyte," *Electrochem. Solid-State Lett.*, vol. 4, no. 8, p. A132, 2001, doi: 10.1149/1.1383429.
- [30] G. H. Newman, R. W. Francis, L. H. Gaines, and B. M. L. Rao, "Hazard Investigations of LiClO<sub>4</sub> / Dioxolane Electrolyte," *J. Electrochem. Soc.*, vol. 127, no. 9, p. 2025, Sep. 1980, doi: 10.1149/1.2130056.
- [31] R. Jasinski and S. Carroll, "Thermal Stability of a Propylene Carbonate Electrolyte," *J. Electrochem. Soc.*, vol. 117, no. 2, p. 218, 1970, doi: 10.1149/1.2407468.
- [32] "Superionic Conductors via Bulk Interfacial Conduction | Journal of the American Chemical Society." <https://pubs.acs.org/doi/10.1021/jacs.0c07060> (accessed Feb. 27, 2021).
- [33] D. L. Comins and S. P. Joseph, "N,N-Dimethylformamide," in *Encyclopedia of Reagents for Organic Synthesis*, American Cancer Society, 2001. doi: 10.1002/047084289X.rd335.
- [34] D. R. Lide, *CRC Handbook of Chemistry and Physics, 85th Edition*. CRC Press, 2004.
- [35] K. Fujii, H. Wakamatsu, Y. Todorov, N. Yoshimoto, and M. Morita, "Structural and Electrochemical Properties of Li Ion Solvation Complexes in the Salt-Concentrated Electrolytes Using an Aprotic Donor Solvent, N, N-Dimethylformamide," *J. Phys. Chem. C*, vol. 120, no. 31, pp. 17196–17204, Aug. 2016, doi: 10.1021/acs.jpcc.6b04542.
- [36] N. B. Colthup, L. H. Daly, and S. E. Wiberley, *Introduction to Infrared and Raman Spectroscopy*, 3rd ed.
- [37] S. B. Lippincott and M. M. Lyman, "Vapor Pressure–Temperature Nomographs," *Ind. Eng. Chem.*, vol. 38, no. 3, pp. 320–323, Mar. 1946, doi: 10.1021/ie50435a022.
- [38] Q.-Y. Wu, X.-N. Chen, L.-S. Wan, and Z.-K. Xu, "Interactions between Polyacrylonitrile and Solvents: Density Functional Theory Study and Two-Dimensional Infrared Correlation Analysis," *J. Phys. Chem. B*, vol. 116, no. 28, pp. 8321–8330, Jul. 2012, doi: 10.1021/jp304167f.
- [39] J. M. Alía and H. G. M. Edwards, "Ion solvation and ion association in lithium trifluoromethanesulfonate solutions in three aprotic solvents. An FT-Raman spectroscopic study," *Vibrational Spectroscopy*, vol. 24, no. 2, pp. 185–200, Dec. 2000, doi: 10.1016/S0924-2031(00)00073-4.
- [40] R. Vargas, J. Garza, D. A. Dixon, and B. P. Hay, "How Strong Is the C $\alpha$ –H $\cdots$ OC Hydrogen Bond?," *J. Am. Chem. Soc.*, vol. 122, no. 19, pp. 4750–4755, May 2000, doi: 10.1021/ja993600a.
- [41] J. Li, X. Huang, and L. Chen, "X-Ray Diffraction and Vibrational Spectroscopic Studies on PAN-LiTFSI Polymer Electrolytes," *J. Electrochem. Soc.*, vol. 147, no. 7, p. 2653, Jul. 2000, doi: 10.1149/1.1393585.